Letter

Tunable Circular Photogalvanic and Photovoltaic Effect in 2D Tellurium with Different Chirality

Chang Niu, Shouyuan Huang, Neil Ghosh, Pukun Tan, Mingyi Wang, Wenzhuo Wu, Xianfan Xu,* and Peide D. Ye*
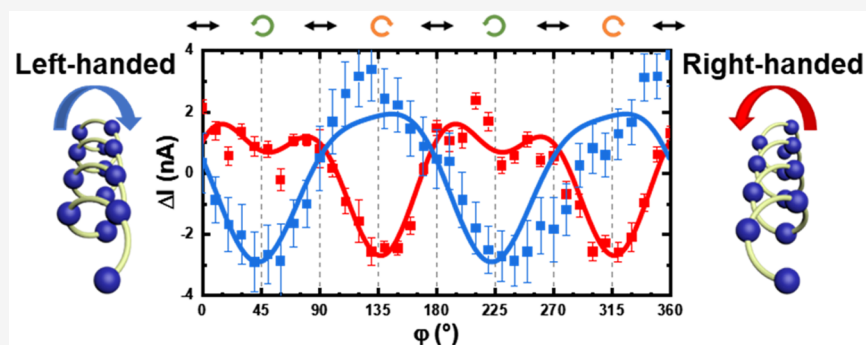
Cite This: https://doi.org/10.1021/acs.nanolett.3c00780

Read Online

ACCESS | Metrics & More | Article Recommendations | Supporting Information

ABSTRACT: Chirality arises from the asymmetry of materials, where two counterparts are the mirror image of each other. The interaction between circular-polarized light and quantum materials is enhanced in chiral space groups due to the structural chirality. Tellurium (Te) possesses the simplest chiral crystal structure, with Te atoms covalently bonded into a spiral atomic chain (left- or right-handed) with a periodicity of 3. Here, we investigate the tunable circular photoelectric responses in 2D Te field-effect transistors with different chirality, including the longitudinal circular photogalvanic effect induced by the radial spin texture (electron-spin polarization parallel to the electron momentum direction) and the circular photovoltaic effect induced by the chiral crystal structure (helical Te atomic chains). Our work demonstrates the controllable manipulation of the chirality degree of freedom in materials.

KEYWORDS: chirality, 2D tellurium, spin texture, circular photogalvanic effect

Chirality is a fundamental property of particles, including electrons,[1] photons, and phonons.[2] The chirality of photons describes the spin angular momentum direction parallel (right-handed) or antiparallel (left-handed) to the light propagation direction. This chirality degree of freedom in light interacts with the electron spin through angular momentum conservation. In solids, the spin—orbit-coupling-induced electron spin polarization required by the crystal symmetry takes various spatial directions, at different momentum directions k, called spin texture. The relation between electron spin texture in chiral materials and circular-polarized light is experimentally discussed using two-dimensional (2D) tellurium (Te) as an example.

Te is an elemental narrow-band-gap semiconductor with a chiral crystal structure.[3] Covalently bonded Te helical atomic chains are arranged in a hexagonal crystal lattice, as illustrated by Figure 1a. Te in a 2D form synthesized by a hydrothermal method[4] shows excellent electrical,[5,6] thermal,[7] and optical[8,9] properties. The chirality of the 2D Te flake is determined by the chirality of the left- or right-handed Te atomic chains, as shown in Figure 1b. Because of the mirror symmetry between

two enantiomers, the asymmetric etch pits[10,11] formed by the hot sulfuric acid etching process can be used to characterize the chirality of 2D Te. The conduction band minimum of Te is located at the corner of the Brillouin zone (H point). Due to the strong spin—orbit interaction[12] and the 3-fold screw symmetry, the spin-splitting conduction bands cross at the H point and form a Weyl node,[13,14] as shown in Figure 1c. The energy dispersion is the same between left- and right-handed Te. However, the topological charge of the Weyl node and the spin polarization of the spin-splitting conduction bands are reversed.[15] 2D Te opens the door for realizing controllable chirality-based spin, electronic, or optical devices.

The spin texture in the Te conduction band is radial[5,16—18] (spin-polarization direction parallel to the electron momentum
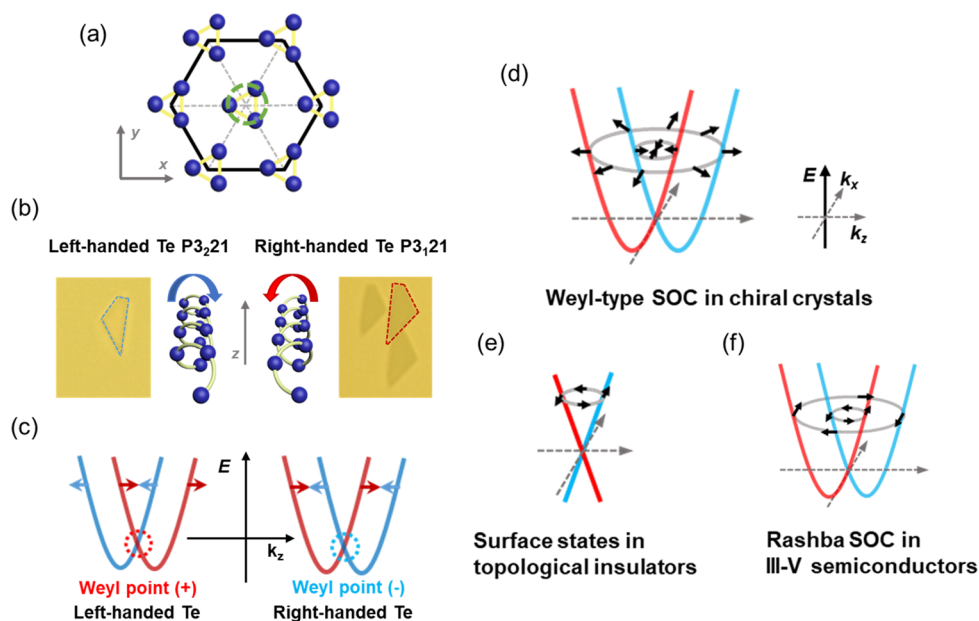
Figure 1. Electron band structure and spin texture of left- and right-handed Te. (a) The crystal structure of Te. (b) The helical Te atomic chains determine the chirality of the Te crystal. Different etch pits are observed in 2D Te after hot sulfuric acid etching. (c) The energy dispersions of left- and right-handed Te are the same. The spin polarization and the Weyl node charge are opposite between the two enantiomers due to the mirror symmetry. The spin texture in various materials: (d) Weyl-type SOC in chiral crystals (spin polarization parallel to momentum direction), (e) surface states in topological insulators (spin polarization perpendicular to momentum direction), and (f) Rashba SOC in III−V semiconductors (spin polarization perpendicular to momentum direction).
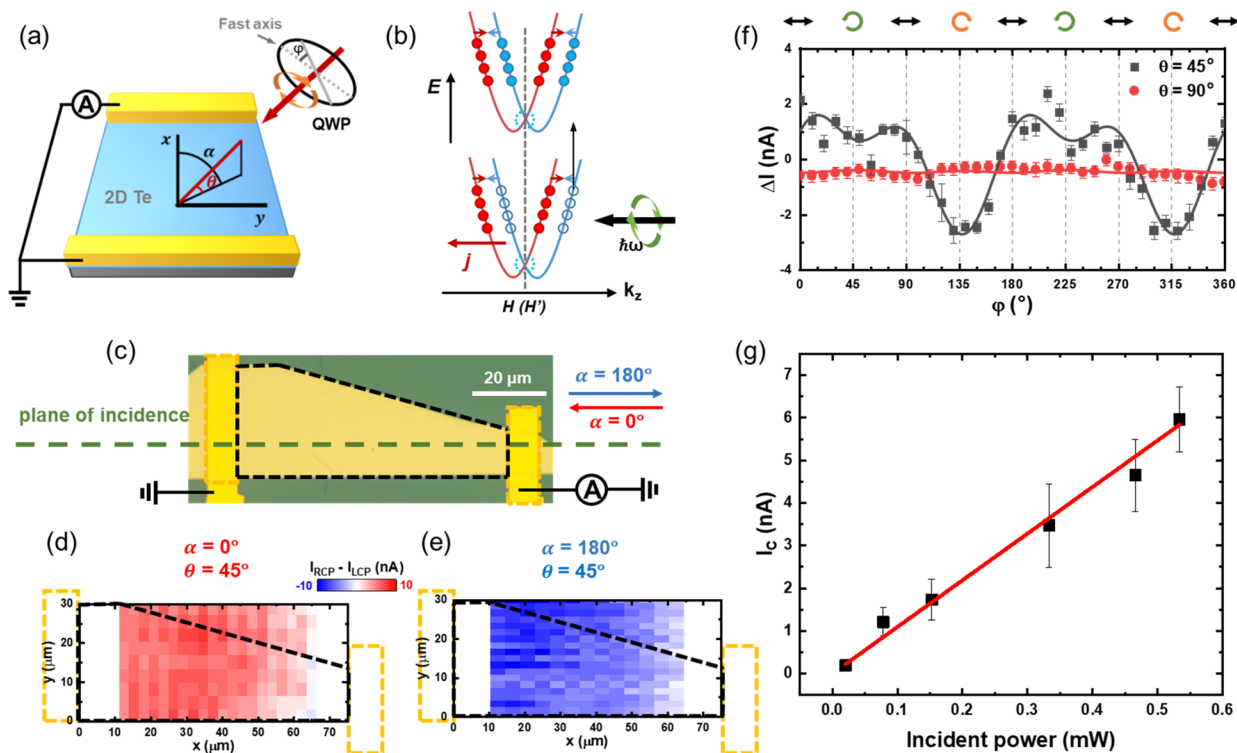

Figure 2. Circular photogalvanic effect in 2D Te. (a) Schematic of the circular-polarized photocurrent measurement setup. (b) The spin-polarized electrical current induced by the circular-polarized light. (c) Optical image of a two-terminal 2D Te field-effect transistor. The green dashed line indicates the plane of incidence. Spatially resolved photocurrent mapping of the difference between right circular-polarized (RCP) light and left circular-polarized light (LCP) under different incident conditions: (d) $\alpha = 0°$, $\theta = 45°$; (e) $\alpha = 180°$, $\theta = 45°$. (f) Photocurrent as a function of the quarter-wave plate angle φ at normally incident light ($\theta = 90°$) and obliquely incident light ($\theta = 45°$). (g) Circular-polarized light-dependent photocurrent I_c as a function of laser intensity I.

direction), as illustrated in Figure 1d. When the Fermi level is over the Weyl node energy, two Fermi surfaces (inner and outer) appear with opposite spin polarization. The spin-polarization direction rotates once around the H point. The
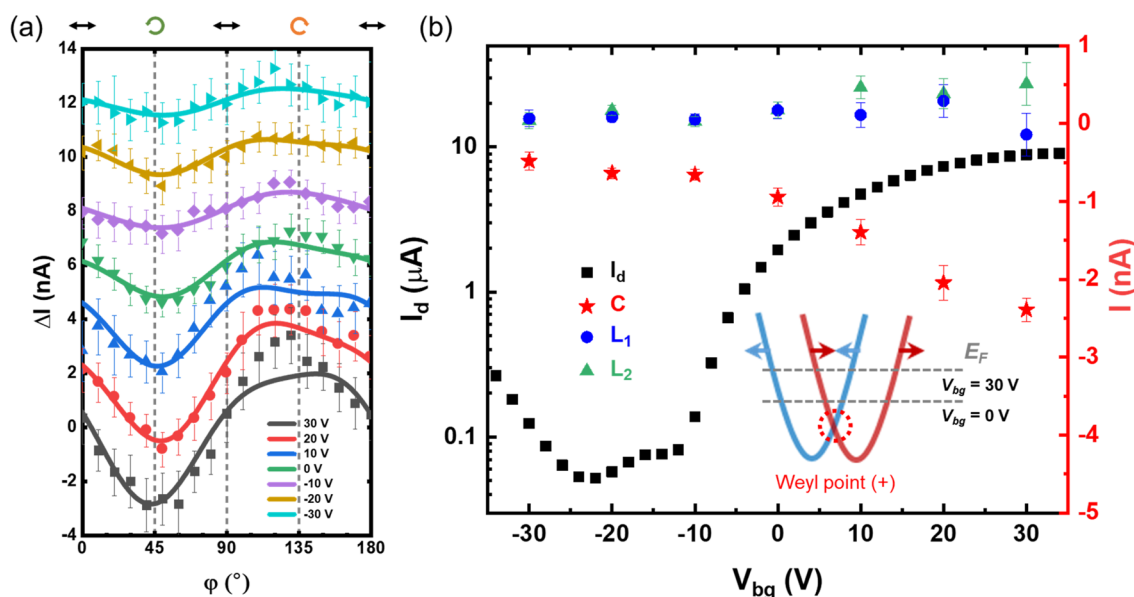
Figure 3. Gate-tunable circular photogalvanic effect in 2D Te. (a) The polarization-dependent photocurrent ΔI as a function of the quarter-wave plate angle φ at different back gate voltages. (b) Output characteristic (black) of a 2D Te field-effect transistor. Fit results calculated from (a): C (red), L_1 (blue), and L_2 (green) as a function of the back gate voltage V_{bg}. Inset in (b): the band structure of 2D Te. The back-gate voltage tunes the Fermi level indicated by the dashed line.

unique radial spin texture originates from the low symmetry of the crystal structure and the strong spin−orbit coupling (SOC) of Te atoms, reflected in the k linear term of the conduction band Hamiltonian[14]

$$H(k) = \frac{\hbar^2 k_\parallel^2}{2m_\parallel} + \frac{\hbar^2 k_\perp^2}{2m_\perp} + \hbar v_\parallel k_\parallel \sigma_z + \hbar v_\perp (k_x \sigma_x + k_y \sigma_y) \tag{1}$$

(eq 1). The Weyl-type SOC-induced[19] radial spin texture is different from that in the surface state of topological insulators[20−22] (Figure 1e, spin-polarization direction perpendicular to the electron momentum direction) or the Rashba SOC of semiconductor interfaces[23] (Figure 1f, spin-polarization direction perpendicular to the electron momentum direction, and two Fermi surfaces with opposite contribution). The left- and right-circular-polarized light with negative and positive angular momentum selectively excite electrons with opposite spin polarizations according to angular momentum conservation. This chiral selection rule leads to the asymmetric populations of electrons with opposite spins, giving rise to a net spin-polarized electrical current.

In this paper, we systematically study the tunable circular optical electronic responses in 2D Te, including the longitudinal circular photogalvanic effect originating from the coupling between circular-polarized light and electron spins and the circular photovoltaic effect as a result of the Te chiral crystal structure. The circular photogalvanic and photovoltaic effects strongly depend on the chirality of the Te crystals, making 2D Te an ideal material system for developing chirality-dependent optoelectronic devices.

■ GATE-TUNABLE LONGITUDINAL CIRCULAR PHOTOGALVANIC EFFECT IN 2D TE

The measurement setup is shown in Figure 2a. In our experiment, a 2D Te field-effect transistor (FET) is illuminated with a 633 nm He-Ne laser (∼7 μm spot size) at room temperature. The polarization-dependent photocurrent was

measured while rotating the quarter-wave plate (QWP) by an angle φ, which altered the laser polarization with a period of 180° from linear polarization (LP) ($\varphi = 0°$) to right circular polarization (RCP) ($\varphi = 45°$), to LP ($\varphi = 90°$), to left circular polarization (LCP) ($\varphi = 135°$), to LP ($\varphi = 180°$). θ is the angle between the incident light direction and $x−y$ plane, α is the angle between the incident plane and x axis (Te atomic chain direction and measured current direction). All of the polarization-dependent photocurrents measured in this paper were under zero source-drain bias ($V_{ds} = 0$ V). As illustrated in Figure 2b, the two Fermi surfaces have opposite spin-polarization directions. The contribution from two Fermi surfaces is opposite. When the circular-polarized light depopulates one branch of the 2D Te conduction band, however, a net spin-polarized current is generated due to the carrier concentration difference. Note that the spin-momentum configuration in 2D Te is different from that in topological insulators and Rashba SOC; the circular photogalvanic effect (CPGE) is longitudinal,[24] where the generated photocurrent direction is parallel to the light incident direction.

Figure 2c is an optical image of a standard two-terminal 2D Te FET. The light is obliquely incident at $\theta = 45°$ along the current measurement direction from opposite directions ($\alpha = 0°$ and 180°). Spatially resolved photocurrent difference ($I_{RCP} − I_{LCP}$) mappings between RCP and LCP light are shown in Figure 2d ($\alpha = 0°$) and Figure 2e ($\alpha = 180°$). The photocurrent is quite uniform in the channel region of the device (which has an area of 30 μm × 75 μm). It has opposite signs under opposite incident light directions, indicating that the longitudinal CPGE originated from the radial spin texture of the 2D Te conduction band. The polarization-dependent photocurrent versus QWP angle φ is described by eq 2[20]

$$I = D + C \sin 2\varphi + L_1 \sin 4\varphi + L_2 \cos 4\varphi \tag{2}$$

where the C term describes the circular polarization sensitive photocurrent with a 180° period, L_1 and L_2 terms depend on the linear polarization of light with a 90° period, and the D
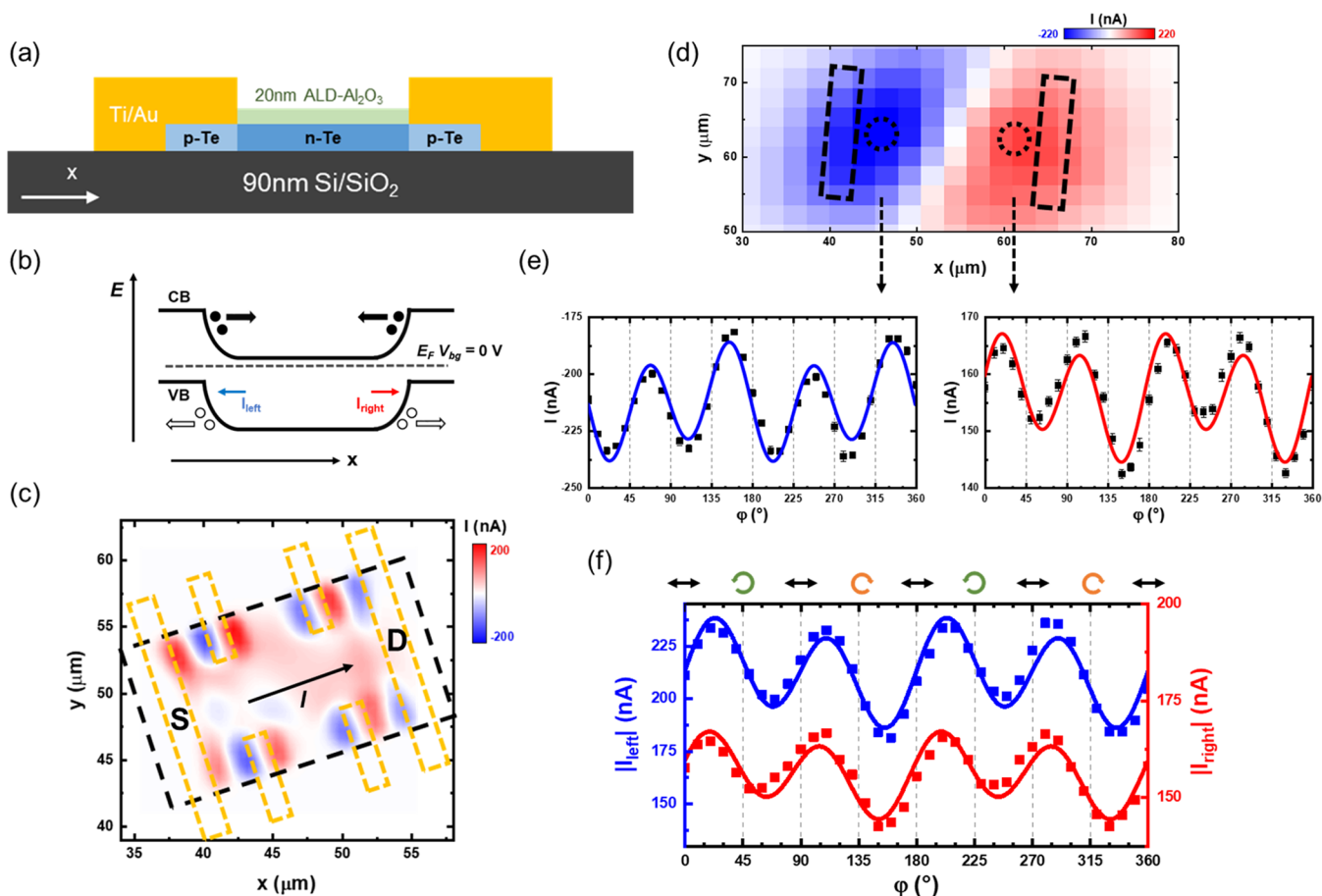
Figure 4. Circular photovoltaic effect in 2D Te. (a) Schematic of the ALD-doped 2D Te device structure. A p−n junction is formed at the edge of the contact due to the different chemical potentials of the 2D Te. (b) Band diagram of the 2D Te field-effect transistor. The direction of the photocurrent is dictated by the built-in field of the p−n junction. (c) Photocurrent mapping of a six-terminal Hall-bar device under normal incident linearly polarized light. (d) Photocurrent mapping of a two-terminal Hall bar device under oblique incident linearly polarized light. (e) Photocurrent as a function of the quarter-wave plate angle φ at left and right contacts. (f) The absolute value of the photocurrent is the same as that shown in (e).

term is the polarization-independent photocurrent. Figure 2f shows the polarization-dependent photocurrent as a function of the QWP angle φ fitted by eq 2 under normal ($\theta = 90°$) and oblique incident light ($\theta = 45°$). The circular polarization sensitive term under oblique incident light is much larger compared to that in normal incident light, which is negligible, again suggesting that the CPGE is sensitive to the electron spin polarization in 2D Te. Furthermore, the polarization-dependent photocurrent is also measured in two orthogonal directions (parallel/perpendicular to the Te atomic chain direction) under oblique incident light at $\theta = 45°$ along the y direction ($\alpha = 90°$), as shown in Figure S1. The dependence of photocurrent on circular-polarized light is negligible when the current measurement direction is perpendicular to the incident plane. In conclusion, the circular-polarization-dependent photocurrent can only be generated along the oblique incident direction due to the radial spin-momentum configuration induced by the Weyl node at the edge of the conduction band. The circular-polarization-dependent photocurrent I_C extracted from eq 2 linearly depends on the power of the incident light, as shown in Figure 2g. The slope is calculated to be 10.9 nA/mW. We excluded the contribution from the circular photon drag effect caused by the linear momentum transfer due to the symmetry requirement of the Te crystal.[25]

Due to the 2D nature of the Te flake, the chemical potential can be easily changed by the field effect. The observed polarization-sensitive photocurrent is tuned by applying a back gate voltage V_{bg}, as shown in Figure 3a. The transfer curve of the 2D Te FET at $V_{ds} = 0.05$ V (black curve in Figure 3b) indicates that the device is operated in the n-type region. The back-gate-dependent photocurrent fitted by eq 2 is shown in Figure 3b. The same tunable circular-polarization-dependent photocurrent is observed in three other different devices, as shown in Figure S2. The value of the C term is a function of the back-gate voltage (electron density). We attribute this tunability to the different scattering rates of carriers under different gate voltages. Because of the unique chiral crystal structure of Te, the negative/positive Weyl nodes are separated in energy, resulting in a large topologically nontrivial window.[19] According to the theoretical prediction, the quantized circular-polarization-dependent saturation photocurrent generated from a single Weyl node is expressed as eq 3[26]

$$I_c^{sat} = -\frac{4\pi\alpha e}{h}IC\tau \tag{3}$$

where α is the fine structure constant, e is the elementary charge, h is the Planck constant, τ is the electron scattering time, I is the intensity of light, and $C = \pm 1$ is the topological
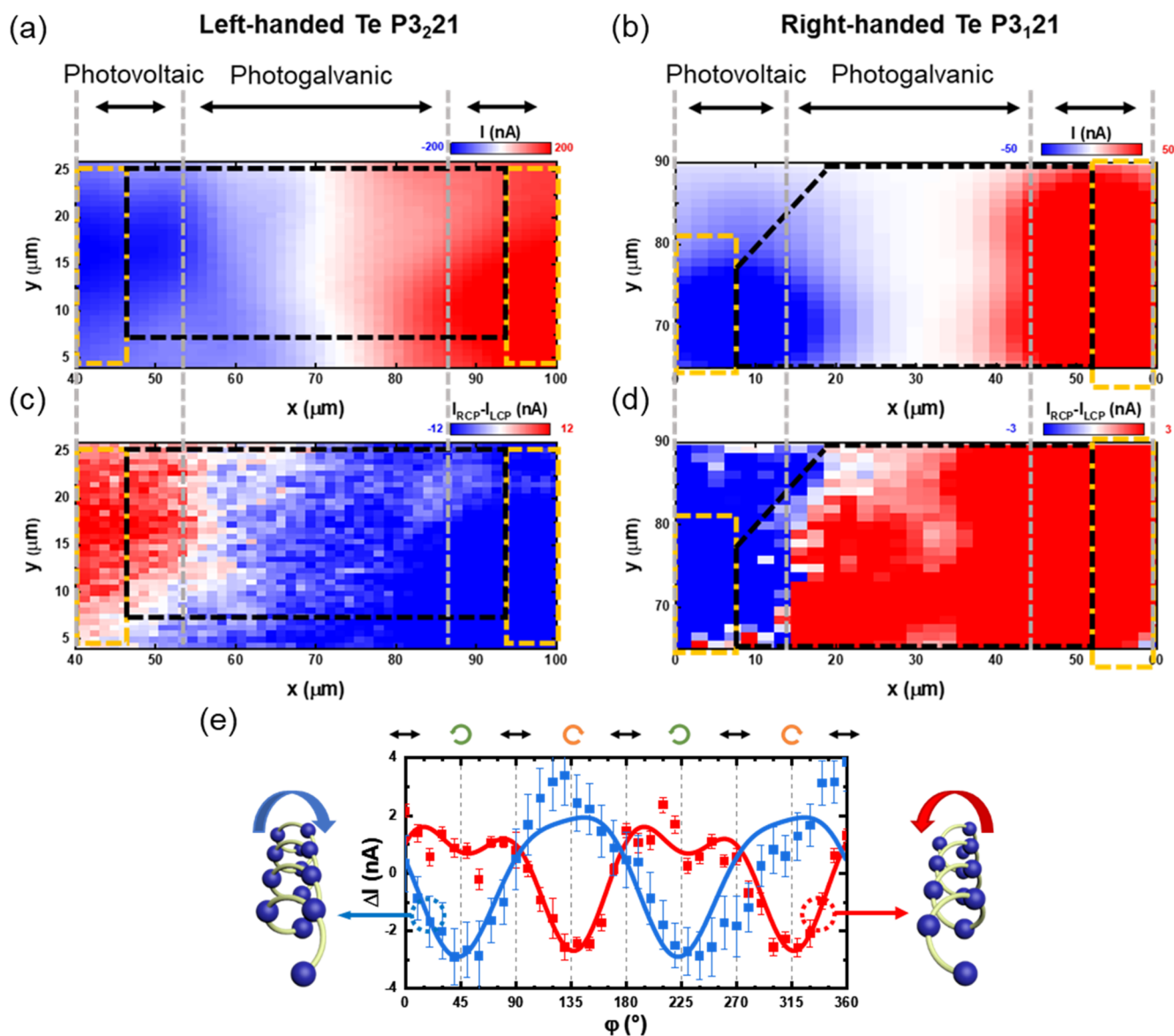
Figure 5. Chirality-dependent circular photogalvanic and photovoltaic effects in 2D Te. (a) Photocurrent mapping of a left-handed 2D Te device under oblique incident linearly polarized light. (b) Photocurrent mapping of a right-handed 2D Te device under the same condition as in (a). (c) Photocurrent difference mapping of a left-handed 2D Te device between oblique incident RCP and LCP light. (d) Photocurrent difference mapping of a right-handed 2D Te device under the same condition as in (c). (e) Polarization-dependent photocurrent as a function of the quarter-wave plate angle φ in left- and right-handed 2D Te.

charge of the Weyl node, which depends on the chirality of the 2D Te crystal, making 2D Te a promising candidate for investigating this exotic phenomenon. In our experiment setup, the photocurrent is measured at the steady-state condition, and the wavelength of the laser falls in the topologically nontrivial energy window. Figure S3 shows the circular-polarization-dependent photocurrent I_c^{sat} as a function of the scattering time estimated using the field-effect mobility $\mu_{FET} = \frac{e}{m^*}\tau$, where m^* is the effective mass. The linear relation in scattering time and incident power indicates the possible topological origin of the CPGE in the 2D Te conduction band.

■ CIRCULAR PHOTOVOLTAIC EFFECT IN 2D TE

Besides the longitudinal CPGE, a circular photovoltaic effect (CPVE) is also observed in a 2D Te FET. The device structure is shown in Figure 4a. A 20 nm thick atomic layer deposition

(ALD) grown Al_2O_3 is used to dope the channel part of the Te flake into an n-type.[27] However, the Te under the contact remains slightly p-doped due to the intrinsic accumulation layer,[28] resulting in a chemical potential difference near the contact. The band diagram of the device is shown in Figure 4b. The electron−hole pairs generated by the incident light are separated by the built-in electric field. The photocurrent has opposite directions at two different contacts. Figure 4c is a photocurrent mapping from normal incident linear-polarized light in a six-terminal Hall-bar 2D Te device. The positive and negative photocurrents generated in the source-drain direction at the edge of each contact indicate the photovoltaic effect in the 2D Te device.

This photovoltaic effect is also polarization-sensitive. Figure 4d is a photocurrent mapping of a two-terminal 2D Te FET under oblique incident linear-polarization light. The polarization-sensitive photocurrent as a function of the QWP angle

φ at two different contacts is shown in Figure 4e. Large opposite circular-polarization-dependent photocurrents C dictated by the p−n junction direction at different contacts are observed. A similar trend is observed in left and right contacts when the absolute value of the photocurrent is plotted (Figure 4f). Unlike the CPGE observed previously, the CPVE photocurrent has a different amplitude in the same direction under LCP and RCP light. It does not depend on the incident angle θ or α (Figure S4), indicating that the CPVE originated from the interaction between polarized light and the chiral crystal structure of 2D Te.[29] In other words, the electron−hole pairs generated by the LCP and RCP light are different. Using the chemical potential difference in the 2D Te homojunction as an amplifier, this difference in LCP and RCP light is enlarged, providing a promising route for circular-polarized light detection.

CHIRALITY-DEPENDENT CIRCULAR PHOTOGALVANIC AND PHOTOVOLTAIC EFFECT

As seen from previous descriptions, circular-polarized light is coupled with electron spins in Te, giving rise to the CPGE, whereas the difference in the populations of the generated electron−hole pairs under LCP and RCP light results in the CPVE. Both effects are chirality-dependent, making 2D Te an ideal platform for chirality-based circular-polarization light detectors.

Figure 5a,b gives photocurrent mappings of left- and right-handed 2D Te devices under oblique incident ($\theta = 45°$) linear-polarization light. The results are similar between the two devices with a negative photocurrent at the left contact and a positive photocurrent at the right contact indicated by the gold dashed squares, because of the photovoltaic effect. Figure 5c,d gives the photocurrent difference ($I_{RCP} - I_{LCP}$) mappings of the same devices under obliquely incident ($\theta = 45°$) LCP and RCP light. Two different regions (near contacts and 2D Te channel) are clearly shown, separated by gray dashed lines. The photocurrent difference generated by LCP and RCP light has opposite signs near two contacts dictated by the p−n junction direction, indicating the CPVE. The CPGE-induced photocurrent difference is nearly uniform across the 2D Te channel. Furthermore, the photocurrent difference is opposite in two enantiomers, indicating that both effects are opposite in 2D Te with different chirality. The polarization-dependent photocurrent measured at the center of the devices as a function of the QWP angle φ in left (blue)- and right-handed (red) 2D Te is plotted in Figure 5e, which clearly shows the opposite CPGE-induced C term caused by 2D Te crystal chirality. This chirality-dependent photocurrent is also observed in other devices with electrons and holes conducting channels, shown in Figures S5−S8. Because electrons (holes) carry negative (positive) charges, the circular-polarization-dependent photocurrent direction reverses when the carrier type is switched. Because of this large chirality dependence of the CPGE and CPVE, it can be envisioned that highly sensitive circular-polarized light detectors can be realized by simultaneously measuring the photogalvanic or the photovoltaic currents in left- and right-handed 2D Te.

In conclusion, we demonstrate two chirality-dependent tunable circular optical electronic responses in a 2D Te FET, including the longitudinal circular photogalvanic effect, which is sensitive to the incident light direction, and the circular photovoltaic effect originating from the intrinsic chiral crystal structure. The strong and controllable coupling between 2D Te and circular-polarized light will enable the realization of chirality-based photodetection and the manipulation of spin and charge current using circular-polarized light.

MATERIALS AND METHODS

Growth of 2D Te Flake. The 2D Te flakes were grown by a hydrothermal method. A 0.09 g portion of Na_2TeO_3 and 0.5 g of polyvinylpyrrolidone (PVP) (Sigma-Aldrich) were dissolved in 33 mL of double-distilled water under magnetic stirring to form a homogeneous solution. A 3.33 mL portion of aqueous ammonia solution (25−28%, w/w%) and 1.67 mL of hydrazine hydrate (80%, w/w%) were added to the solution. The mixture was sealed in a 50 mL Teflon-lined stainless steel autoclave and heated at 180 °C for 30 h before naturally cooling it to room temperature.

Device Fabrication. Te flakes were transferred onto a 90 nm SiO_2/Si substrate. The six-terminal Hall-bar devices were patterned using two-step electron beam lithography, where 20/60 nm Ti/Au metal contacts were deposited by electron beam evaporation. A 20 nm amount of ALD Al_2O_3 was deposited onto the Te flakes at 200 °C using $(CH_3)_3Al$ (TMA) and H_2O as precursors.

Hot Sulfuric Acid Etching of the 2D Te Flakes. The synthesized 2D Te flakes were transferred onto a 90 nm SiO_2/Si substrate. 2D Te flakes were cleaned following a DI water rinse and a standard solvent cleaning process (acetone, methanol, and isopropanol). 2D Te flakes were etched in hot concentrated sulfuric acid at 100 °C for 5 min.

Circular Polarized Photocurrent Measurements. A 633 nm He-Ne laser beam was focused using an objective (Mitutoyo 10× M Plan Apo) to a spot size of ∼7 μm and an incident angle of 45°. The laser spot was scanned along the channel of the device using a piezoelectric nanopositioner. A quarter-wave plate (QWP) was used to control the polarization of the beam. The photocurrent was measured using a DC source meter (Keithley 2612A). All measurements were performed at zero source-drain bias and room temperature.

ASSOCIATED CONTENT

Ⓢ Supporting Information

The Supporting Information is available free of charge at https://pubs.acs.org/doi/10.1021/acs.nanolett.3c00780.

> Additional data and details of the photocurrent measured at transverse incident light, the relation between saturation photocurrent and electron scattering time, gate voltage dependence of circular-polarization-dependent photocurrent, the photovoltaic effect under normal incident light, and chirality-dependent photocurrent mapping of hole and electron conducting channels (PDF)

AUTHOR INFORMATION

Corresponding Authors

Xianfan Xu − *Elmore Family School of Electrical and Computer Engineering, Purdue University, West Lafayette, Indiana 47907, United States; Birck Nanotechnology Center and School of Mechanical Engineering, Purdue University, West Lafayette, Indiana 47907, United States;* ⓞ orcid.org/0000-0003-0580-4625; Email: xxu@ecn.purdue.edu

Peide D. Ye − *Elmore Family School of Electrical and Computer Engineering, Purdue University, West Lafayette, Indiana 47907, United States; Birck Nanotechnology Center,*

Purdue University, West Lafayette, Indiana 47907, United States; ⓞ orcid.org/0000-0001-8466-9745; Email: yep@purdue.edu

Authors

Chang Niu − *Elmore Family School of Electrical and Computer Engineering, Purdue University, West Lafayette, Indiana 47907, United States; Birck Nanotechnology Center, Purdue University, West Lafayette, Indiana 47907, United States;* ⓞ orcid.org/0000-0003-3175-7164

Shouyuan Huang − *Birck Nanotechnology Center and School of Mechanical Engineering, Purdue University, West Lafayette, Indiana 47907, United States*

Neil Ghosh − *Birck Nanotechnology Center and School of Mechanical Engineering, Purdue University, West Lafayette, Indiana 47907, United States*

Pukun Tan − *Elmore Family School of Electrical and Computer Engineering, Purdue University, West Lafayette, Indiana 47907, United States; Birck Nanotechnology Center, Purdue University, West Lafayette, Indiana 47907, United States*

Mingyi Wang − *School of Industrial Engineering, Purdue University, West Lafayette, Indiana 47907, United States*

Wenzhuo Wu − *School of Industrial Engineering, Purdue University, West Lafayette, Indiana 47907, United States;* ⓞ orcid.org/0000-0003-0362-6650

Complete contact information is available at:
https://pubs.acs.org/10.1021/acs.nanolett.3c00780

Author Contributions

P.D.Y. conceived and supervised the project. C.N. designed the experiments. C.N., S.H., and N.G. performed the photocurrent measurements under the supervision of X.X. M.W. synthesized the material under the supervision of W.W. C.N. and P.T. performed the hot sulfuric acid etching and fabricated the devices. C.N. and S.H. analyzed the data. C.N. wrote the manuscript, and all of the authors commented on it.

Notes

The authors declare no competing financial interest.

◼ REFERENCES

(1) Hasan, M. Z.; Xu, S. Y.; Belopolski, I.; Huang, S. M. Discovery of Weyl Fermion Semimetals and Topological Fermi Arc States. *Annu. Rev. Condens. Matter Phys.* **2017**, *8*, 289−309.

(2) Zhu, H.; Yi, J.; Li, M. Y.; Xiao, J.; Zhang, L.; Yang, C. W.; Kaindl, R. A.; Li, L. J.; Wang, Y.; Zhang, X. Observation of Chiral Phonons. *Science* **2018**, *359* (6375), 579−582.

(3) Bradley, A. J. The Crystal Structures of the Rhombohedral Forms of Selenium and Tellurium. *London, Edinburgh, and Dublin Philosophical Magazine and Journal of Science* **1924**, *48*, 477−496.

(4) Wang, Y.; Qiu, G.; Wang, R.; Huang, S.; Wang, Q.; Liu, Y.; Du, Y.; Goddard, W. A.; Kim, M. J.; Xu, X.; et al. Field-Effect Transistors Made from Solution-Grown Two-Dimensional Tellurene. *Nat. Electron.* **2018**, *1* (4), 228−236.

(5) Qiu, G.; Niu, C.; Wang, Y.; Si, M.; Zhang, Z.; Wu, W.; Ye, P. D. Quantum Hall Effect of Weyl Fermions in N-Type Semiconducting Tellurene. *Nat. Nanotechnol.* **2020**, *15* (7), 585−591.

(6) Niu, C.; Qiu, G.; Wang, Y.; Si, M.; Wu, W.; Ye, P. D. Bilayer Quantum Hall States in an N-Type Wide Tellurium Quantum Well. *Nano Lett.* **2021**, *21* (18), 7527−7533.

(7) Huang, S.; Segovia, M.; Yang, X.; Koh, Y. R.; Wang, Y.; Ye, P. D.; Wu, W.; Shakouri, A.; Ruan, X.; Xu, X. Anisotropic Thermal Conductivity in 2D Tellurium. *2D Mater.* **2020**, *7* (1), 015008.

(8) Amani, M.; Tan, C.; Zhang, G.; Zhao, C.; Bullock, J.; Song, X.; Kim, H.; Shrestha, V. R.; Gao, Y.; Crozier, K. B.; et al. Solution-Synthesized High-Mobility Tellurium Nanoflakes for Short-Wave Infrared Photodetectors. *ACS Nano* **2018**, *12* (7), 7253−7263.

(9) Ma, J.; Cheng, B.; Li, L.; Fan, Z.; Mu, H.; Lai, J.; Song, X.; Yang, D.; Cheng, J.; Wang, Z.; et al. Unveiling Weyl-Related Optical Responses in Semiconducting Tellurium by Mid-Infrared Circular Photogalvanic Effect. *Nat. Commun.* **2022**, *13* (1), 1−7.

(10) Koma, A.; Tanaka, S. Etch Pits and Crystal Structure of Tellurium. *Phys. Status Solidi* **1970**, *40* (1), 239−248.

(11) Niu, C.; Qiu, G.; Wang, Y.; Jian, J.; Wang, H.; Wu, W.; Ye, P. D. Tunable Nonreciprocal Electrical Transport in 2D Tellurium with Different Chirality. *arXiv* 2022. arXiv:2201.08829.

(12) Niu, C.; Qiu, G.; Wang, Y.; Zhang, Z.; Si, M.; Wu, W.; Ye, P. D. Gate-Tunable Strong Spin-Orbit Interaction in Two-Dimensional Tellurium Probed by Weak Antilocalization. *Phys. Rev. B* **2020**, *101* (20), 205414.

(13) Hirayama, M.; Okugawa, R.; Ishibashi, S.; Murakami, S.; Miyake, T. Weyl Node and Spin Texture in Trigonal Tellurium and Selenium. *Phys. Rev. Lett.* **2015**, *114* (20), 206401.

(14) Tsirkin, S. S.; Puente, P. A.; Souza, I. Gyrotropic Effects in Trigonal Tellurium Studied from First Principles. *Phys. Rev. B* **2018**, *97* (3), 035158.

(15) Schröter, N. B. M.; Stolz, S.; Manna, K.; De Juan, F.; Vergniory, M. G.; Krieger, J. A.; Pei, D.; Schmitt, T.; Dudin, P.; Kim, T. K.; et al. Observation and Control of Maximal Chern Numbers in a Chiral Topological Semimetal. *Science* **2020**, *369* (6500), 179−183.

(16) Hirayama, M.; Okugawa, R.; Ishibashi, S.; Murakami, S.; Miyake, T. Weyl Node and Spin Texture in Trigonal Tellurium and Selenium. *Phys. Rev. Lett.* **2015**, *114* (20), 206401.

(17) Gatti, G.; Gosálbez-Martínez, D.; Tsirkin, S. S.; Fanciulli, M.; Puppin, M.; Polishchuk, S.; Moser, S.; Testa, L.; Martino, E.; Roth, S.; et al. Radial Spin Texture of the Weyl Fermions in Chiral Tellurium. *Phys. Rev. Lett.* **2020**, *125* (21), 216402.

(18) Sakano, M.; Hirayama, M.; Takahashi, T.; Akebi, S.; Nakayama, M.; Kuroda, K.; Taguchi, K.; Yoshikawa, T.; Miyamoto, K.; Okuda, T.; et al. Radial Spin Texture in Elemental Tellurium with Chiral Crystal Structure. *Phys. Rev. Lett.* **2020**, *124* (13), 136404.

(19) Chang, G.; Wieder, B. J.; Schindler, F.; Sanchez, D. S.; Belopolski, I.; Huang, S. M.; Singh, B.; Wu, D.; Chang, T. R.; Neupert, T.; et al. Topological Quantum Properties of Chiral Crystals. *Nat. Mater.* **2018**, *17* (11), 978−985.

(20) McIver, J. W.; Hsieh, D.; Steinberg, H.; Jarillo-Herrero, P.; Gedik, N. Control over Topological Insulator Photocurrents with Light Polarization. *Nat. Nanotechnol.* **2012**, *7* (2), 96−100.

(21) Huang, S.; Xu, X. Optical Chirality Detection Using a Topological Insulator Transistor. *Adv. Opt. Mater.* **2021**, *9* (10), 2002210.

(22) Huang, S.; Miotkowski, I.; Chen, Y. P.; Xu, X. Deep Tuning of Photo-Thermoelectricity in Topological Surface States. *Sci. Rep.* **2020**, *10* (1), 16761.

(23) Wang, S.; Zhang, H.; Zhang, J.; Li, S.; Luo, D.; Wang, J.; Jin, K.; Sun, J. Circular Photogalvanic Effect in Oxide Two-Dimensional Electron Gases. *Phys. Rev. Lett.* **2022**, *128* (18), 187401.

(24) Ni, Z.; Wang, K.; Zhang, Y.; Pozo, O.; Xu, B.; Han, X.; Manna, K.; Paglione, J.; Felser, C.; Grushin, A. G.; et al. Giant Topological Longitudinal Circular Photo-Galvanic Effect in the Chiral Multifold Semimetal CoSi. *Nat. Commun.* **2021**, *12* (1), 145.

(25) Shalygin, V. A.; Moldavskaya, M. D.; Danilov, S. N.; Farbshtein, I. I.; Golub, L. E. Circular photon drag effect in bulk tellurium. *Phys. Rev. B* **2016**, *93* (4), 045207.

(26) De Juan, F.; Grushin, A. G.; Morimoto, T.; Moore, J. E. Quantized Circular Photogalvanic Effect in Weyl Semimetals. *Nat. Commun.* **2017**, *8* (1), 15995.

(27) Qiu, G.; Si, M.; Wang, Y.; Lyu, X.; Wu, W.; Ye, P. D. High-Performance Few-Layer Tellurium CMOS Devices Enabled by Atomic Layer Deposited Dielectric Doping Technique. In *Device Research Conference - Conference Digest, DRC*; 2018.

(28) Berezovets, V. A.; Farbshtein, I. I.; Shelankov, A. L. Weak localization under lifted spin-degeneracy conditions (two-dimensional layer on a tellurium surface). *JETP Lett.* **1984**, *39*, 2.

(29) Nomura, K. C. Optical activity in tellurium. *Phys. Rev. Lett.* **1960**, *5* (11), 500.